Electrocatalysis of Anodic Oxygen-Transfer Reactions: $Bi_3Ru_3O_{11}$ Electrodes in Acidic Media

Lin He,† Jeff R. Anderson, Hugo F. Franzen,* and Dennis C. Johnson*

Department of Chemistry and Ames Laboratory, Iowa State University, Ames, Iowa 50011

Received August 2, 1996. Revised Manuscript Received November 13, 1996⊗

Details are reported for the synthesis and characterization of composite materials prepared from powdered $Bi_3Ru_3O_{11}$ and a polymeric adhesive fashioned into disk electrodes. The structure of the synthesized material was found to be that of the cubic $KSbO_3$ type on the basis of single-crystal and powder X-ray diffractometry. The surface morphology of a composite electrode was determined to be quite porous on the basis of micrographs obtained using scanning electron microscopy. Voltammetric data obtained for various anodic reactions at these electrodes were examined for evidence that oxidations can occur with transfer of oxygen to the oxidation products in the potential region corresponding to onset of anodic discharge of H_2O. Model reactants include iodide, dimethyl sulfoxide, tetramethylene sulfoxide, and manganese(II). The electronic band structure of $Bi_3Ru_3O_{11}$ was calculated; it was concluded that mixing of Ru 4d and O 2p orbitals in an antibonding band at the Fermi level facilitates oxygen transfer.

Introduction

The electrochemical oxidation of species in aqueous solution, with transfer of oxygen atoms from H_2O to the oxidation product(s), has significant potential as a technique for both the synthesis and the degradation of substances in aqueous solution. The efficiencies of electrode reactions, as determined by their overpotentials, depend upon the mechanisms of the reactions, which in turn depend upon the chemical nature of the electrodes. It has been proposed that the principal reaction in anodic O-transfer reactions involving dissolved species is the transfer of oxygen from an adsorbed OH species that is produced by oxidation of water, as indicated by reactions I and II

$$S[\,] + H_2O \rightarrow S[OH] + H^+ + e^- \qquad (I)$$

$$S[OH] + R \rightarrow S[\,] + RO + H^+ + e^- \qquad (II)$$

where S[ ] = a vacant surface site, S[OH] = adsorbed OH, R = reactant, and RO = product.[1−5] The OH species generated in reaction I also is an intermediate product in the anodic evolution of O_2 by mechanisms depicted in reactions III and IV. Hence, desired O-

$$2S[OH] \rightarrow 2S[\,] + O_2 + 2H^+ + 2e^- \qquad (III)$$

$$S[OH] + H_2O \rightarrow S[\,] + O_2 + 3H^+ + 3e^- \qquad (IV)$$

transfer reactions are expected always to occur with concomitant evolution of some O_2. Thus, the maximization of current efficiency for the desired O-transfer reactions is a major challenge in this work. We expect that current efficiencies will be maximized for anode materials that offer a relatively low density of adsorption sites and for which the rates of reactions III and IV are small relative to the rate of reaction II.

A large number of studies of electrode oxidations have been carried out on noble metals (which are, under oxidizing conditions, coated with an oxide layer) and more recently on conducting oxides. The study reported here was undertaken to examine the oxidation reactions on anodes consisting of the compound $Bi_3Ru_3O_{11}$. The purpose of this study was to discover the nature of the oxidation reactions, if any, on this ternary material. One motivation for the selection of this material is that the comparatively oxygen-deficient compound, $Bi_2Ru_2O_7$, is known to be a metallic conductor[6,7] that anodically oxidizes water extensively at potentials in excess of 0.6 V (vs Hg/HgO) with negligible decomposition of the electrode.[8−10]

A second motivation stems from the assumptions that solid surfaces have unsatisfied valences and that transition metals in such surfaces would present empty d orbitals that can be active in catalysis. These assumptions lead directly to the consideration of $Bi_3Ru_3O_{11}$ as an electrocatalyst, i.e., d orbitals on Ru presumably would be free to bind OH, thereby partially oxidizing coordinately unsaturated Ru at the surface (reaction I). This species is in turn available for the transfer of an oxygen atom to the solution species (reaction II). These reaction steps are relatively facile when d orbitals contribute to a relatively broad, free-electron-like conduction band, and thus the oxidation state changes at the surface are delocalized over the whole solid. The motivation, then, is to examine the Ru contribution to

* Co-correspondents.
† Present address: 108 Roxalana Hills Drive, Dunbar, WV 25064.
⊗ Abstract published in *Advance ACS Abstracts,* February 15, 1997.
(1) Yeo, I.-H.; Kim, S.; Jacobson, R. A.; Johnson, D. C. *J. Electrochem. Soc.* **1989**, *136*, 1395.
(2) Hsiao, Y.-L.; Johnson, D. C. *J. Electrochem. Soc.* **1989**, *136*, 3704.
(3) Johnson, D. C.; Chang, H.; Feng, J.; Wang, W. In *Electrochemistry for a Cleaner Environment*; Genders, J. D., Weinberg, N. L., Eds.; The Electrosynthesis Co., Inc.: East Amherst, NY, 1992; Chapter 17.
(4) Vitt, J. E.; Johnson, D. C. *J. Electrochem. Soc.* **1992**, *139*, 774.
(5) Comninellis, Ch. *Electrochim. Acta* **1994**, *39*, 1857.
(6) Kanno, R.; Takeda, Y.; Yamamoto, T.; Kawamoto, Y.; Yamamoto, O. *J. Solid State Chem.* **1993**, *102*, 106.
(7) Cox, P. A.; Goodenough, J. B.; Tavener, P. J.; Telles, D. *J. Solid State Chem.* **1986**, *62*, 360.

S0897-4756(96)00415-2 CCC: $14.00

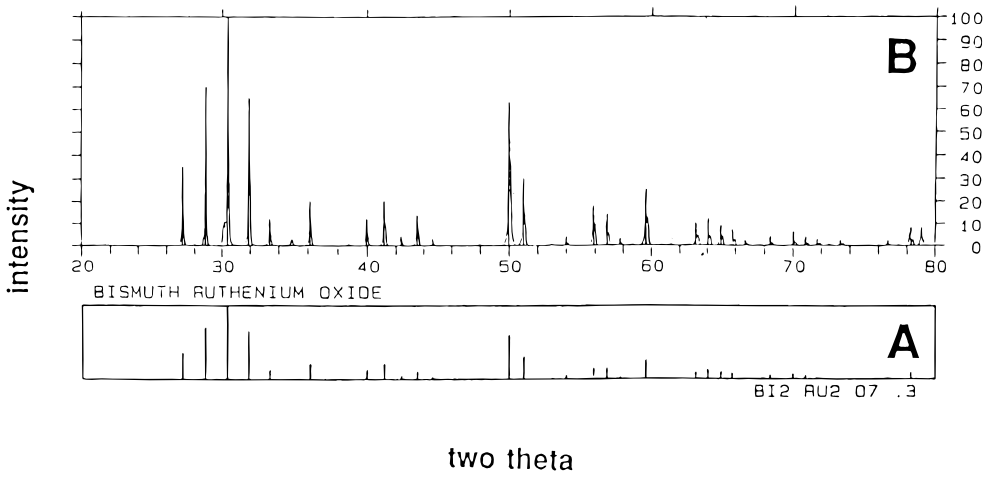

Figure 1. X-ray powder diffraction patterns: (A) theoretical for $Bi_3Ru_3O_{11}$, (B) prepared powdered sample.

Table 1. Atomic Coordinates for $Bi_3Ru_3O_{11}$[a]

atom	site	*x*	*y*	*z*
Ru	12*g*	3/4	1/4	−0.1114(5)
Bi(1)	8*e*	0.3841(2)	0.1159(2)	0.1159(2)
Bi(2)	4*b*	0	0	0
O(1)	12*f*	0.585(4)	1/4	1/4
O(2)	8*e*	0.146(3)	*x*	*x*
O(3)	24*h*	0.105(2)	0.032(3)	−0.246(3)

[a] Space group *Pn*3, origin choice 2, $a = 9.2961$ Å.

the electronic states of the solid in relationship to the known conductivity and observed electrocatalytic activity of this material.

Iodide is considered as an ideal model reactant in the characterization of new electrode materials because two anodic reactions have been observed for this ion at noble-metal electrodes in acidic media: (i) the oxidation of I^- to I_2 (1 equiv mol^{-1}) by a quasi-reversible process with $E_{1/2}$ = ca. 0.5 V vs SCE, and (ii) the oxidation of I^- to IO_3^- (6 equiv mol^{-1}) by an irreversible process with a variable $E_{1/2}$ that has been correlated with the overpotential for anodic discharge of H_2O at several noble metals and glassy carbon (GC).[4] Dimethyl sulfoxide (DMSO) and tetramethylene sulfoxide (TMSO) also are good model reactants because the expected oxidations to the corresponding sulfones ($DMSO_2$ and $TMSO_2$) have relatively simple stoichiometries involving transfer of single oxygen atoms. Furthermore, $E°$ values for the $DMSO_2$−DMSO and $TMSO_2$−TMSO redox couples are ca. 0.0 V vs SCE,[11] and therefore the corresponding oxidations of DMSO and TMSO are thermodynamically allowed at potentials easily accessible at common anode materials (Pt, Au, PbO_2, and GC); however, these reactions are not observed to occur persistently at these anodes.[12] The anodic oxidation of Mn^{2+} is examined because multiple O-transfer steps are likely to be associated with production of MnO_2(s) and/or MnO_4^-.

Experimental Details

Reagents. Standard solutions were prepared from reagent grade chemicals: KI (Fisher Scientific), DMSO (Fisher), TMSO (Aldrich), and $Mn(NO_3)_2$ (Sigma). The supporting electrolyte was 0.10 M H_2SO_4 (Mallinckrodt). Water was purified by distillation followed by passage through two D-45 deionizing columns (Culligan) and a Milli-Q system (Millipore).

Electrodes. A mixture of the appropriate amounts of Bi_2O_3 and RuO_2 (Alfa, Johnson Matthey) was ground in an agate mortar and then pressed into the form of a pellet by a laboratory press (Carver) at an applied pressure of 5 tons cm^{-2}. Pelletization improved contact between particles and, thereby, increased the diffusion rate during thermal treatment. The pellet was placed in a small Pt crucible located in the quartz tube of a resistance furnace. The pellet was annealed in air at 600 °C for 18 h, 700 °C for 24 h, and 800 °C for 72 h under the control of an 818 Controller/Programmer (Eurotherm).

After thermal processing, the pellet was ground to a fine powder and blended with a polymeric cement (Duco) to produce a conductive paste. The paste was spread over one end of a stainless steel rod to be used as a rotated disk electrode (RDE) with a geometric area (A_{geom}) of 0.264 cm^2. The cylindrical surface of the rod then was covered with pure cement (Duco) and, after curing, was wrapped with Teflon tape to prevent contact between the stainless steel and test solutions. Two disk electrodes were prepared using different ratios of polymer-to-$Bi_3Ru_3O_{11}$ powder. RDE-I was made from a 1:1 (vol:vol) mixture of polymer and Bi_3RuO_{11} and RDE-II was made from a 2:1 (vol:vol) mixture. Finally, the faces of the disk electrodes were polished very lightly with 1-μm alumina on microcloth (Buehler) using water as the lubricant. Only the disk electrode surfaces were allowed to contact test solutions during use.

Instrumentation. X-ray diffractometry (XRD) was performed using an XDS-2000 diffractometer (Scintag) with Cu $K\alpha_1$ radiation. Single-crystal data were collected on a rotating anode, four-circle diffractometer (Rigaku AFC6R) using monochromatic Mo Kα radiation. The crystal structure was solved using SHELXS[13] and TEXSAN[14] software. Scanning electron microscopy (SEM) was performed using a S-200 (Cambridge) equipped with a thin-window energy-dispersive detector (Tracor Northern). X-ray photoelectron spectroscopy (XPS) was performed using a Perkin-Elmer 5500 multitechnique surface analysis system (Physical Electronics) with monochromatic Al Kα radiation (1486.6 eV, 300 W) for excitation. Binding energies were referenced to the O(1s) emission band at 531 eV,[15] and the difference in binding energy between O(1s) and $Ru(3d_{5/2})$ was 247 eV. The base pressure of the ion-pumped ultrahigh vacuum (UHV) chamber was less than 1×10^{-9} Torr during analysis.

(8) Horowitz, H. S.; Longo, J. M.; Horowitz, H. H.; Lewandowski, J. T. In *Solid State Chemistry in Catalysis*; Grasselli, R. K., Brazdil, J. F., Eds.; ACS Symposium Series 279, American Chemical Society: Washington, DC, 1985; p 143.
(9) Horowitz, H. S.; Longo, J. M.; Horowitz, H. H. *J. Electrochem. Soc.* **1983**, *130*, 1851.
(10) Marković, N. M.; Ross, P. N., Jr. *J. Electrochem. Soc.* **1994**, *141*, 2590.
(11) *Standard Potentials in Aqueous Solution*; Bard, A. J., Parsons, R., Jordan, J., Eds.; Marcel Dekker: New York, 1985.
(12) Chang, H.; Johnson, D. C. *J. Electrochem. Soc.* **1990**, *137*, 2452.
(13) Sheldrick, G. M. *SHELXS-86*, Universität Göttingen, Germany.
(14) TEXSAN: *Single-Crystal Structure Analysis Software, Version 5.0*, Molecular Structure Corp.: The Woodlands, TX, 1989.
(15) *Handbook of X-ray Photoelectron Spectroscopy*; Chastain, J., Ed.; Perkin-Elmer Corporation: Eden Prairie, MN, 1992.

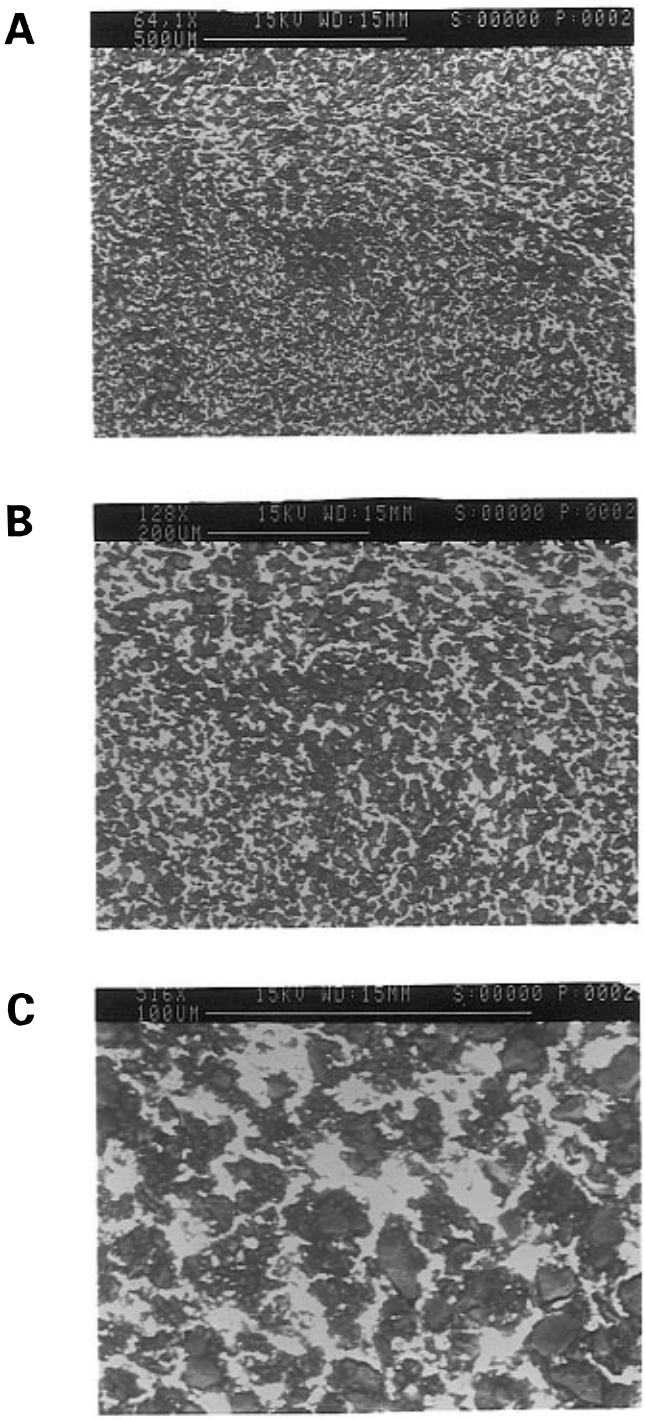

Figure 2. Scanning electron micrographs of the composite surface of RDE-I.

Voltammetry was performed using a RDE4 potentiostat and AFMSRX rotator (Pine Instrument) interfaced with a 486 personal computer (Apex) by a DT2800-A data acquisition board (Data Translation) under the control of ASYST-3.1 software (Keithley/ASYST). The electrochemical cell had porous glass disks separating the working, reference, and counter electrode compartments. All potentials are reported in volts vs a saturated calomel electrode (SCE, Fisher Scientific). The counter electrode was a Pt wire.

Voltammetric Procedures. Background-corrected electrode currents (Δi) were taken from so-called difference voltammograms ($\Delta i - E$) calculated by subtraction of the $i-E$ responses obtained in the presence and absence of reactants. These difference calculations are anticipated to discriminate against background currents resulting from double-layer charging, formation, and dissolution of surface oxides and the anodic and cathodic evolution of O_2 and H_2, respectively.[16]

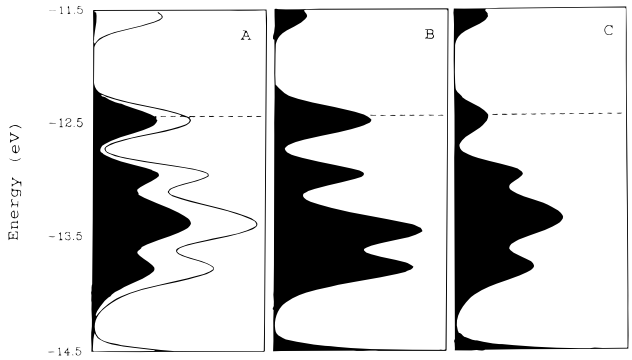

Figure 3. (A) Total DOS (solid line) and partial Ru DOS (shaded area), (B) partial DOS of O(1), (C) partial DOS of O(3). The Fermi level is represented by the dashed line.

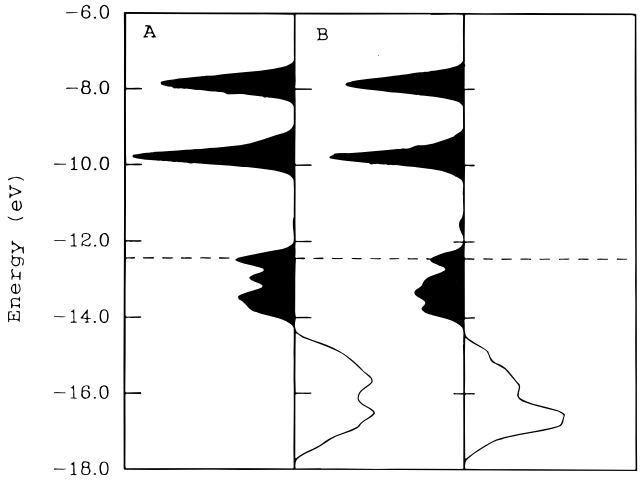

Figure 4. COOP curves: (A) Ru−O(1) bond, (B) Ru−O(3) bond. Fermi level is represented by the dashed line. Shaded areas are antibonding.

Values for the effective number of electrons (n_{eff}, equiv mol^{-1}) transferred in electrode processes were estimated from the slopes of plots of Δi (mA) vs the square root of the angular velocity of electrode rotation ($\omega^{1/2}$, $\text{rad}^{1/2}\ \text{s}^{-1/2}$), according to the Levich equation[17] given by eq V, where A_{geom} is the geometric electrode area (cm^2), D is the diffusion coefficient of the reactant ($\text{cm}^2\ \text{s}^{-1}$), ν is the solution kinematic viscosity ($\text{cm}^2\ \text{s}^{-1}$), and F and C^b have their usual electrochemical significance.

$$i = 0.62 n_{\text{eff}} F A_{\text{geom}} D^{2/3} \nu^{-1/6} \omega^{1/2} C^b \qquad \text{(V)}$$

Results and Discussion

XRD, Single Crystal, and SEM Data. The structure of the synthesized compound, $Bi_3Ru_3O_{11}$, was confirmed by direct comparison of both XRD and single-crystal data. Figure 1 contains the XRD data obtained for the mixed metal oxide powder prepared in this study (B) in comparison with the calculated pattern for $Bi_3Ru_3O_{11}$ (A).[18] Single-crystal studies show that the synthesized compound crystallizes in the space group $Pn3$, with $a = 9.2961$ Å, and the calculated atomic positions as listed in Table 1. Direct comparison of these atomic positions with previously reported single-crystal[19] and neutron[20] diffraction studies confirm that the synthesized material is the ternary compound

(16) Noel, M.; Vasu, K. I. *Cyclic Voltammetry and the Frontiers of Electrochemistry*, Aspect Publications Ltd.: London, 1990; p 24.
(17) Levich, V. G. *Physicochemical Hydrodynamics*, Prentice Hall, Inc.: Englewood Cliffs, NJ, 1962; pp 62−70.
(18) JCPDS (File 26-222) International Center for Diffraction Data, 1601 Park Lane: Swarthmore, PA, 1992.

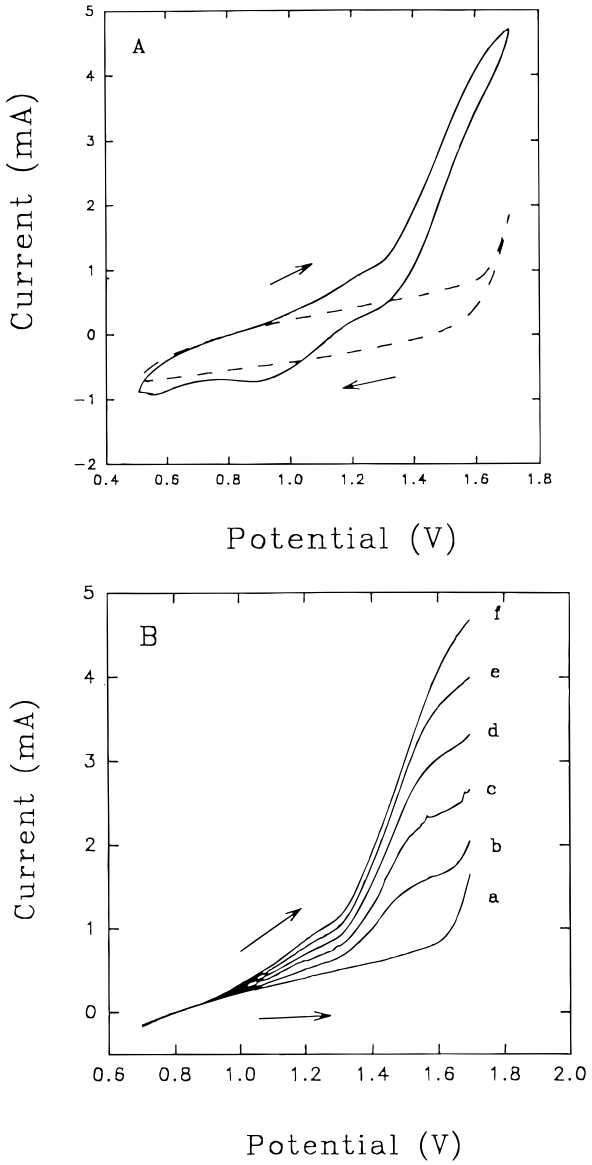

Figure 5. Cyclic voltammetric response (A) for 2.5 mM I^- and linear-scan voltammetric response (B) as a function of I^- concentration in 0.10 M H_2SO_4. Curves: (- - -) background, (—) with I^-. Concentration of I^- in B (mM): (a) 0, (b) 0.5, (c) 1.0, (d) 1.5, (e) 2.0, (f) 2.5. Electrode: RDE-II. Rotational velocity: 168 rad s^{-1}. Scan rate: 30 mV s^{-1}.

designated as $Bi_3Ru_3O_{11}$. The average grain size for the material represented by Figure 1B is estimated to be ca. 0.7 μm on the basis of the Fresnel construction.[21]

The planar surface of the electrode designated RDE-I, prepared from the material represented in Figure 1B, was examined using SEM and micrographs taken at different magnifications are shown in Figure 2. The appearance of this composite material is that expected of a nearly homogeneous 1:1 mixture of conductive $Bi_3Ru_3O_{11}$ particles and clusters (black, 0.1−10-μm cross section) within a nonconductive (white) matrix of the polymeric adhesive. The existence of some porosity is evident for RDE-I in Figure 2C; however, porosity was much less evident for RDE-II (micrograph not shown) which was prepared with a 2:1 polymer-to-$Bi_3Ru_3O_{11}$ ratio.

(19) Abraham, F.; Nowogrocki, G.; Thomas, D. *C. R. Acad. Sci. Fr., Ser. C* **1975**, 279.
(20) Facer, G. R.; Elcombe, M. M.; Kennedy, B. J. *Aust. J. Chem.* **1993**, *46*, 1897.
(21) Guinier, A. *X-ray Diffraction*; W. H. Freeman and Co.: San Francisco, 1963; p 121.

Electronic Band Structure. The electronic band structure of $Bi_3Ru_3O_{11}$ has been calculated by the extended Hückel method. Figure 3A shows the total DOS curve along with the partial DOS of Ru. Figure 3B,C contain the partial DOS plot for the oxygen sites O(1) and O(3), respectively. The bands between approximately −2.0 and −14.5 eV are comprised mainly of Ru 4d orbitals with some contribution from the oxygen 2p orbitals. The partial DOS curves for both of the Bi sites and the oxygen O(2) site (not shown) reveal no significant density between −2.0 and −4.5 eV. COOP curves for the Ru−O bonds (Figure 4A,B) show that the occupied band at the Fermi level is moderately antibonding.

Anodic Response for Iodide. Figure 5A contains $i-E$ curves obtained with RDE-II in 0.10 M H_2SO_4 containing 2.5 mM I^- (—) in comparison with the background response (- - -). Anodic discharge of H_2O with evolution of O_2 is readily observed for this current sensitivity to occur in the background curve for $E > 1.6$ V in this acidic medium. The anodic wave with $E_{1/2}$ = ca. 1.1 V is concluded to correspond to the oxidation of I^- to I_2. Whereas this $E_{1/2}$ value is considerably more positive than values observed for the same reaction at noble metal electrodes ($E_{1/2}$ = ca. 0.5 V at Pt, Ir, and Au), this $E_{1/2}$ is close to the value of 1.0 V observed at glassy carbon electrodes.[4] The larger anodic wave with $E_{1/2}$ = ca. 1.5 V is concluded tentatively to correspond to the oxidation of I^- to IO_3^-. This wave originates in the approximate potential region for onset of H_2O discharge and appears to reach a maximum current for $E >$ ca. 1.6 V where the rate of H_2O discharge is significant. The background-corrected wave height for IO_3^- production is independent of scan direction and scan rate (curves not shown), and therefore this wave can be concluded not to include a contribution from oxidative desorption of I^- and/or I^0 that is adsorbed at $E < 1.3$ V.

Figure 5B contains $i-E$ curves recorded for the positive scan as a function of I^- concentration in the range 0.50−2.5 mM. Values of Δi calculated for oxidation of I^- to I_2 at $E = 1.2$ V from the data shown in Figure 5B were determined to be a linear function of I^- concentration ($r = 0.999$) which is an indication that this process occurs with fast heterogeneous kinetics. Most significant in Figure 5B is evidence that $E_{1/2}$ for oxidation of I^- to IO_3^- shifts to increasingly positive values as the I^- concentration is increased. This is evidence that increasing values of I^- flux require increasing rates of H_2O discharge to produce the flux of OH species required to support the transport-limited oxidation of I^- to IO_3^-. As a consequence, the appearance of a current plateau becomes increasingly obscure as the I^- concentration is increased because of an increasing contribution to the total current response from the concomitant evolution of O_2. The value of $E_{1/2}$ for IO_3^- production at RDE-I (data not shown) was ca. 1.1 V for 2.5 mM I^-. Differences between $E_{1/2}$ values observed for the two electrodes are discussed in a later section.

Figure 6 contains plots of the maximum values of Δi vs $\omega^{1/2}$ corresponding to oxidation of 0.50 mM I^- at 1.2 V (curve A) and at 1.6 V (curve B) for RDE-II. The plots are linear with regression statistics given by $\Delta i = a + b\omega^{1/2}$, with $a = 0.025$ mA and $b = 0.0070$ mA rad$^{-1/2}$ s$^{1/2}$ ($r = 0.996$) for curve A (1.2 V), and $a = 0.091$ mA

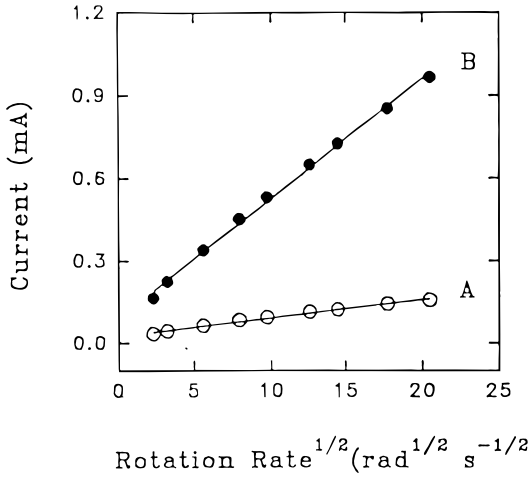

Figure 6. Levich plots of background-corrected currents at RDE-II for oxidation of 0.50 mM I^- in 0.1 M H_2SO_4. Potential (V vs SCE): (A) 1.20, (B) 1.59.

and $b = 0.043$ mA rad$^{-1/2}$ s$^{1/2}$ ($r = 0.999$) for curve B (1.6 V). The linearity of these $\Delta i - \omega^{1/2}$ plots is an indication that the corresponding anodic processes occur at transport-limited rates at the potentials designated. The ratio of the slopes for the two plots in Figure 6, i.e., 0.043/0.0070 = 6.1, is in good agreement with the expected value of $n_{\text{eff,1.6V}}/n_{\text{eff,1.2V}} = 6$ corresponding to transport-limited oxidations of I^- to IO_3^- (1.6 V) and I_2 (1.2 V). This result confirms our speculation above that the anodic reaction with $E_{1/2}$ = ca. 1.5 V in Figure 5A corresponds to the oxidation of I^- to IO_3^-.

Anodic Response for DMSO and TMSO. Oxidations of DMSO and TMSO to $DMSO_2$ and $TMSO_2$, respectively, are thermodynamically allowed at potentials accessible at the common anode materials (Pt, Au, PbO_2, and C); however, these reactions are not observed to occur persistently at these anodes.[12] Figure 7A contains the $i-E$ curve obtained at RDE-II in 0.10 M H_2SO_4 containing 5.0 mM DMSO (—) in comparison to the background response (- - -). The anodic wave with $E_{1/2}$ = ca. 1.5 V, originating in the potential region corresponding approximately to the onset of anodic discharge of H_2O, is concluded tentatively to correspond to oxidation of DMSO to $DMSO_2$. Figure 7B contains $i-E$ curves (positive scan) as a function of DMSO concentration in the range 5−15 mM which demonstrate that $E_{1/2}$ for DMSO oxidation shifts to more positive values as concentration is increased. As discussed for the anodic wave corresponding to oxidation of I^- to IO_3^- (Figure 5B), this behavior is expected for an anodic O-transfer reaction that requires simultaneous discharge of H_2O.

Figure 8 contains a plot of the maximum values of Δi vs $\omega^{1/2}$ for oxidation of 1.0 mM DMSO at ca. 1.6 V for RDE-II. The nonlinearity of this plot is interpreted to be evidence that the reaction occurs under mixed control by heterogeneous kinetics and convective-diffusional mass transport. Regression statistics of the linear segment ($\omega^{1/2}$ < ca. 6 rad$^{1/2}$ s$^{-1/2}$) shown with a zero intercept in Figure 8 are indicated by $\Delta i = b\omega^{1/2}$, where $b = 0.037$ mA rad$^{-1/2}$ s$^{1/2}$ ($r = 0.992$). The value $n_{\text{eff}} = 2.3$ equiv mol^{-1} is calculated from the slope using $A_{\text{geom}} = 0.264$ cm^2, and the generic values $\nu = 0.010$ cm^2 s^{-1} and $D = 1.0 \times 10^{-5}$ cm^2 s^{-1}. Given these approximations for ν and D, this value for n_{eff} is considered to be in good agreement with the tentative conclusion that

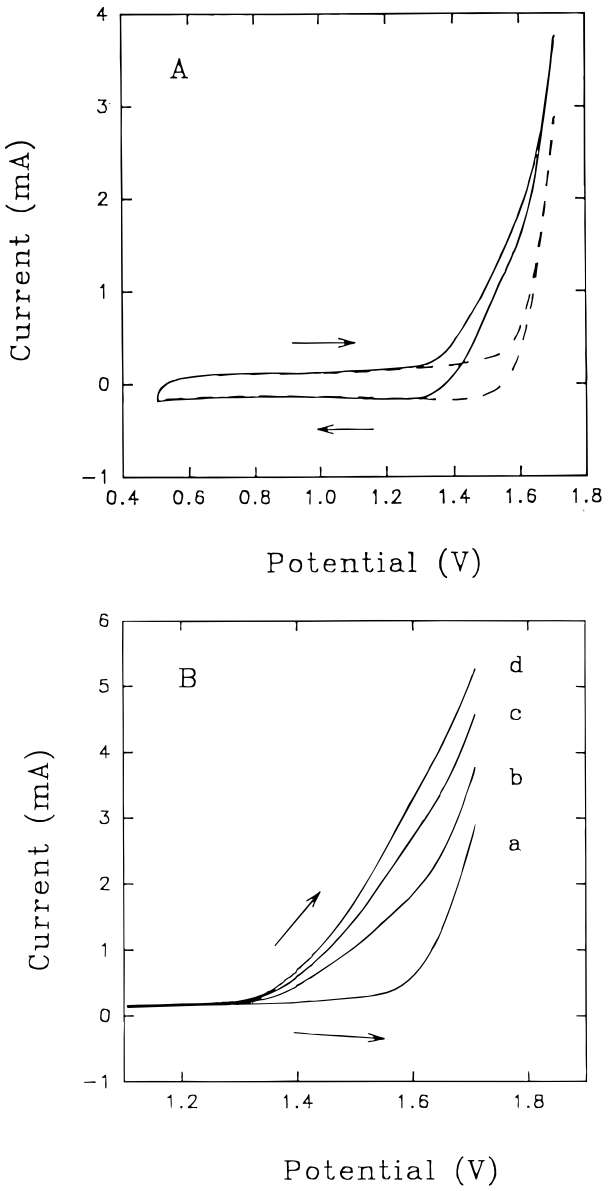

Figure 7. Cyclic voltammetric response (A) for 5.0 mM DMSO and linear-scan voltammetric response (B) as a function of DMSO concentration in 0.10 M H_2SO_4. Curves: (- - -) background, (—) with DMSO. Concentration of DMSO in B (mM): (a) 0, (b) 5, (c) 10, (d) 15. Electrode: RDE-II. Rotational velocity: 168 rad s^{-1}. Scan rate: 30 mV s^{-1}.

the reaction at 1.6 V corresponds to the oxidation of DMSO to $DMSO_2$ (2 equiv mol^{-1}).

Figure 9A contains $i-E$ data obtained at RDE-II in 0.10 M H_2SO_4 with (—) and without (- - -) the presence of 5.0 mM TMSO. The anodic wave with $E_{1/2}$ = ca. 1.6 V is concluded to correspond to the oxidation of TMSO to $TMSO_2$. Figure 9B contains $i-E$ curves (positive scan) as a function of TMSO concentration. Again, as in Figure 7B for DMSO, the $E_{1/2}$ shifts to more positive values with increasing concentration, as is expected now for anodic O-transfer reaction. Figure 10 contains a plot of the maximum values of Δi, calculated at ca. 1.7 V vs $\omega^{1/2}$ for oxidation of 2.0 mM TMSO at RDE-II. The nonlinear plot is evidence that the reaction occurs under mixed kinetic-transport control. Regression statistics for the linear segment shown in Figure 10 with a zero intercept ($\omega^{1/2}$ < ca. 6 rad$^{1/2}$ s$^{-1/2}$) are indicated by $i = b\omega^{1/2}$ where $b = 0.070$ mA rad$^{-1/2}$ s$^{1/2}$. From this slope, the value $n_{\text{eff}} = 2.2$ equiv mol^{-1} is calculated using $A_{\text{geom}} = 0.264$ cm^2, and the generic values $\nu = 0.010$ cm^2 s^{-1}

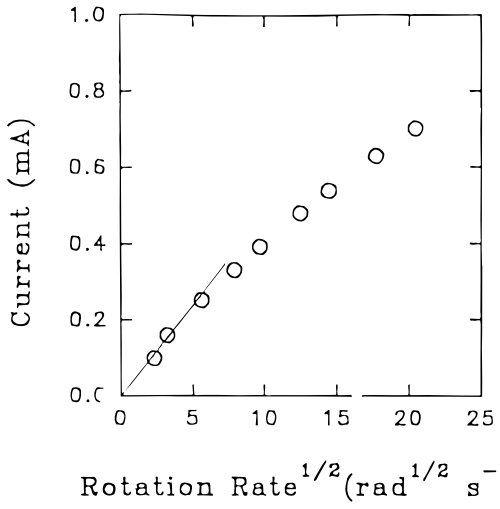

Figure 8. Levich plots of maximum background-corrected currents at electrode RDE-II for oxidation of 1.0 mM DMSO at ca. 1.60 V in 0.10 M H_2SO_4.

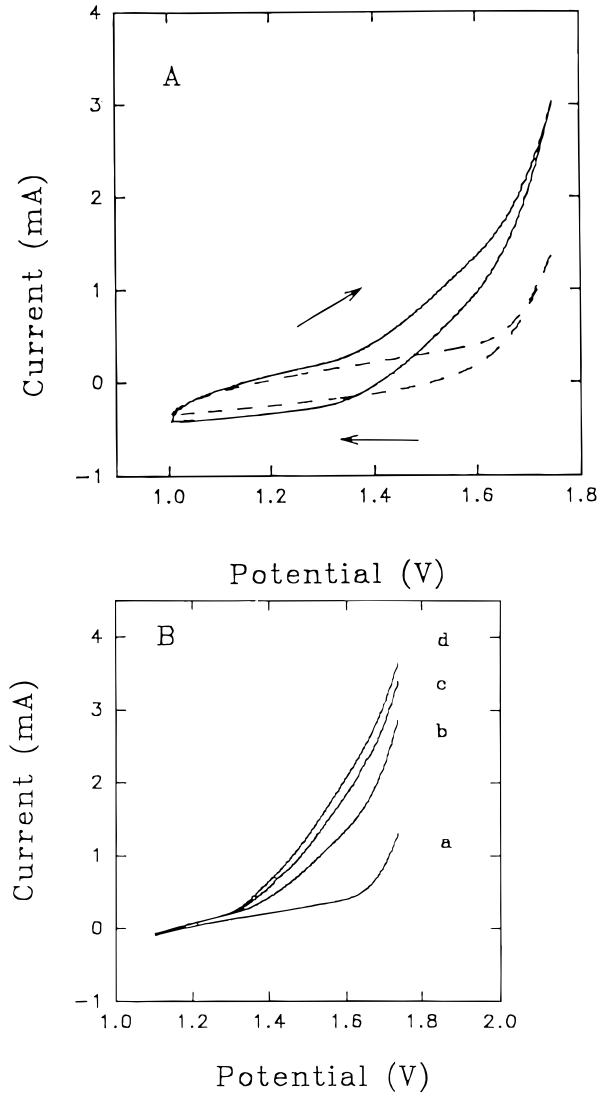

Figure 9. Cyclic voltammetric response (A) for 5.0 mM TMSO and linear-scan voltammetric response (B) as a function of TMSO concentration in 0.10 M H_2SO_4. Curves: (- − - -) background, (——) with DMSO. Concentration of DMSO in B (mM): (a) 0, (b) 5, (c) 10, (d) 15. Electrode: RDE-II. Rotational velocity: 168 rad s^{-1}. Scan rate: 30 mV s^{-1}.

and $D = 1.0 \times 10^{-5}$ cm^2 s^{-1}. This value of n_{eff} is consistent with the conclusion that TMSO is oxidized

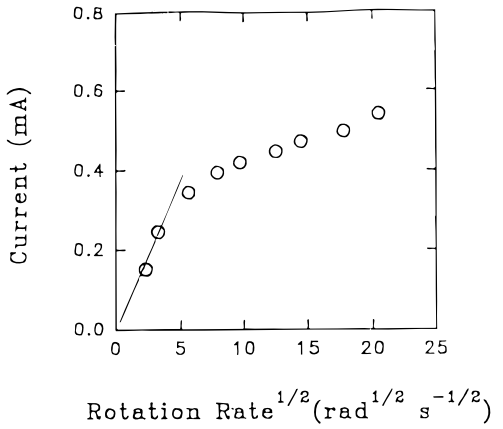

Figure 10. Levich plots of maximum background-corrected current at RDE-II for oxidation of 2.0 mM TMSO at ca. 1.7 V in 0.10 M H_2SO_4.

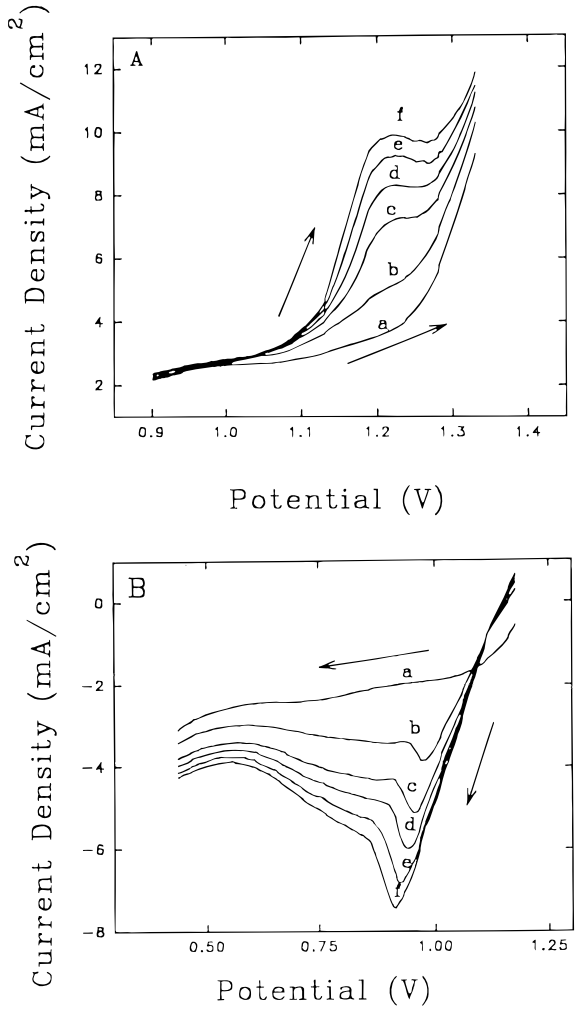

Figure 11. Cyclic voltammetric response for Mn(II) at RDE-I obtained for the positive (A) and negative (B) scans as a function of Mn(II) concentration in 0.10 M H_2SO_4. Concentration of Mn(II) (mM): (a) 0, (b) 10, (c) 20, (d) 30, (e) 40, (f) 50. Rotational velocity: 168 rad s^{-1}. Scan rate: 30 mV s^{-1}.

to $TMSO_2$ (2 equiv mol^{-1}) at 1.7 V.

Values of $E_{1/2}$ for oxidation of DMSO and TMSO in 0.10 M H_2SO_4 at RDE-I (data not shown) were determined to be 1.15 and 1.05 V, respectively.

Anodic Response for Mn^{2+}. Figure 11 contains $i-E$ curves for the positive (A) and negative (B) scans at RDE-I in 0.10 M H_2SO_4 as a function Mn^{2+} concentration in the range 10−50 mM (Figure 11b−f). The

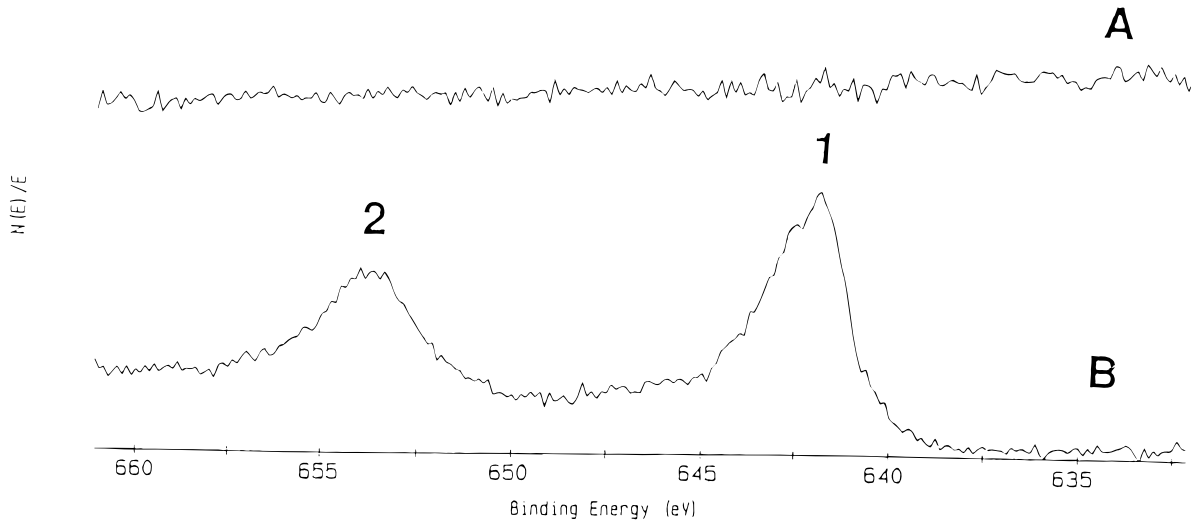

Figure 12. XPS spectra before (A) and after (B) electrolysis at 1.24 V on RDE-I for 2 h in 0.1 M H_2SO_4 containing 50 mM Mn(II).

background response is shown for comparison (Figure 11a). Anodic discharge of H_2O with evolution of O_2 is readily observed at the sensitivity used to record Figure 11a to occur at $E >$ ca. 1.2 V. The anodic current for O_2 evolution in Figure 11A is larger than that in Figure 7A because the smaller polymer content of the composite material in RDE-I (Figure 11A) results in greater surface porosity and, therefore, a larger active area for this composite electrode. The anodic wave with $E_{1/2} =$ ca. 1.15 V observed for the positive scan in curves b−f (Figure 11A) results from Mn^{2+} oxidation; however, the appearance of the cathodic peak ($E_{peak} =$ ca. 0.9 V) during the negative scan in Figure 11B is evidence that the product of Mn^{2+} oxidation is an insoluble material, probably MnO_2(s), deposited on the electrode surface. This conclusion is supported by the observation that the area under the cathodic peak increases as a function of increasing Mn^{2+} concentration (Figure 11B). This conclusion is supported also by data (not shown) in which the area of the cathodic peak was determined to increase as a function of time spent at $E = 1.2$ V when the potential scan was interrupted at this potential.

A solution containing 50 mM Mn^{2+} was electrolyzed for a 2-h period at RDE-I for constant values of $E = 1.2$ V and $\omega = 168$ rad s^{-1}. There was no evidence for the formation of purple MnO_4^- in the test solution during the electrolysis. Following this electrolysis period, the electrode was removed from the test solution, rinsed with deionized water and examined by XPS. Figure 12 contains XPS results obtained before (A) and after (B) the 2-hr electrolysis period. Peaks 1 and 2 (Figure 12B) correspond to binding energies of 642 and 654 eV, respectively, which match the reported values for MnO_2(s) at 642.2 eV ($2p_{3/2}$) and 653.9 eV ($2p_{1/2}$) but not those values for MnO_4^- at 646.6 eV and 657 eV.[15] Hence, we conclude that MnO_2(s) is the exclusive product of Mn^{2+} oxidation under these conditions.

Conclusions

The linearity of plots of Δi vs $\omega^{1/2}$ for oxidation of I^- to I_2 and to IO_3^- at RDE-II (Figure 4) is evidence that substantial overlap exists between the diffusion zones of adjacent microelectrodes. Hence, under these conditions, the composite electrodes respond analogously to uniformly accessible rotated disk electrodes instead of microelectrode arrays.

Table 2. Comparison of Experimental $E_{1/2}$ and Thermodynamic $E°$ Values

reactions (0.10 M H_2SO_4)	$E°_{ox,red}$ (V vs SCE)	$E_{1/2}$ (V vs SCE) RDE-I[a]	$E_{1/2}$ (V vs SCE) RDE-II[a]
$I^- \rightarrow IO_3^-$	0.79 [22]	1.1	1.5
$DMSO \rightarrow DMSO_2$	−0.07 [22]	1.15	1.45
$TMSO \rightarrow TMSO_2$	−0.1 [11,23]	1.05	1.56
$Mn^{2+} \rightarrow MnO_2$(s)	0.86 [22]	1.13	n.a.

[a] Rotational velocity: 168 rad s^{-1}.

It is the foremost premise of this research that anodic discharge of H_2O to produce adsorbed OH radicals according to reaction I is a prerequisite of anodic O-transfer reactions. Hence, voltammetric waves for anodic O-transfer reactions are expected to have similar $E_{1/2}$ values which correlate with the onset of O_2 evolution. This premise is supported by data summarized in Table 2 which were obtained at the two electrodes examined. The $E_{1/2}$ values for the specified anodic reactions at the separate electrodes are similar despite large differences in the corresponding standard redox potentials ($E°$). However, the averages of these $E_{1/2}$ values for the individual electrodes are substantially different, i.e., ca. 1.1 V for RDE-I and ca. 1.5 V for RDE-II. Nevertheless, this difference of ca. 0.4 V correlates with the difference in potential corresponding to a minimum observable rate of O_2 evolution, i.e., ca. 1.2 V for RDE-I (see Figure 11) and ca. 1.6 V at RDE-II (see Figure 5A). This difference in apparent O_2 evolution overpotential is concluded to be a consequence of the difference in active surface areas resulting from the differing amounts of polymer used in preparation of the two composite electrodes. For these composite electrodes, the polymer-to-$Bi_3Ru_3O_{11}$ ratio was 1:1 for RDE-I and 2:1 for RDE-II. Hence, the active surface area (A_{act}) corresponding to exposed $Bi_3Ru_3O_{11}$ particles is larger in RDE-I than in RDE-II. This fact is substantiated by the observation that the background current in the region 0.8−1.2 V, concluded to result from double-layer charging, is approximately 5 times larger at RDE-I (Figure 11) than at RDE-II (Figure 5). The flux density for OH species generated by reaction I is proportional to A_{act}; however, the flux density of reactant species being transported to the rotated electrode is proportional to the geometric area (A_{geom}) which is identical for the two electrodes. Hence, the smaller value of the area ratio A_{act}/A_{geom} for RDE-II results in a positive shift

in $E_{1/2}$ values for anodic O-transfer reactions in comparison to RDE-I. The variation of $E_{1/2}$ with changes in the ratio A_{act}/A_{geom} requires further study; however, the present procedure for preparation of composite materials as illustrated by these results does not provide sufficient control of A_{act} to support such a study at this time.

A very substantial difference is observed between $E_{1/2}$ values for oxidation of I^- to I_2 at $Bi_3Ru_3O_{11}$ composite electrodes (ca. 1.1 V, see Figure 5) and at Pt electrodes (ca. 0.5 V). We noted above the absence of variation in the anodic current for IO_3^- production as a result of variation in the potential scan rate. This is evidence that oxidative desorption of adsorbed I^- and/or I^0 does not contribute to the rate of IO_3^- production. We speculate, on this basis, that adsorption of I^- and/or I^0 does not occur and, furthermore, that the absence of these absorptions results in the irreversibility of the oxidation of I^- to I_2 at the $Bi_3Ru_3O_{11}$ electrode material. Furthermore, the oxidation of I^- to IO_3^- also occurs at the onset of H_2O discharge without any evidence for adsorption of the reactant in this O-transfer reaction.

It is disappointing that MnO_2(s), instead of MnO_4^-, is observed to be the product of Mn^{2+} oxidation at $Bi_3Ru_3O_{11}$ composite electrodes. A similar observation was reported for the $Bi^{5+}-Pb^{4+}$ mixed-oxide electrodes. More specifically, virtually no Mn^{2+} oxidation occurs at pure PbO_2 electrodes and only MnO_4^- is generated at transport-limited rates at the mixed-oxide electrodes containing a Bi^{5+}/Pb^{4+} ratio of ca. 1. However, some MnO_2(s) is generated simultaneously with MnO_4^- for mixed-oxide electrodes containing $0 < Bi^{5+}/Pb^{4+} \ll 1$. In the later case, accumulation of MnO_2(s) resulted to fouling of the electrode with cessation of further oxidation of Mn^{2+}.[24] Hence, we conclude for the $Bi_3Ru_3O_{11}$ electrode, that the surface activity of adsorbed OH species is sufficient to support production of MnO_2(s) but not MnO_4^-, even at relatively large positive potentials for which the rate of H_2O discharge is large, and therefore the flux of OH radicals would seem to be adequate to support the O-transfer reaction. This is possibly a result of the OH species interacting with a band at the Fermi level in an antibonding fashion, resulting in the OH species not being absorbed with sufficient stability to ensure a lifetime that is adequate to support the mechanism for MnO_4^- production. Hence, the effective surface activity of adsorbed OH is small despite a substantial rate of OH generation.

Finally, the fact that $Bi_3Ru_3O_{11}$ composite electrodes exhibit sufficient electrocatalytic activity to support the anodic O-transfer reactions for DMSO and TMSO, whereas these reactions are not observed at the common anode materials (Au, Pt, PbO_2, GC) lends support to the idea, presented in the Introduction, that the Ru 4d bands between −12.0 and −14.5 eV, are active in the electrocatalysis of the O-transfer mechanisms tested here.

Acknowledgment. ESCA data were obtained by James W. Anderegg. Extended Hückel calculations were carried out using a tight binding program written by Gordon J. Miller. Ames Laboratory is operated for the U.S. Department of Energy by Iowa State University under Contract No. W-7405-ENG-82. This research was supported by the Director for Energy Research, Office of Basic Energy Sciences.

CM960415C

(22) *Tables of Standard Electrode Potentials*; Milazzo, G., Carol, S., Eds.; John Wiley and Sons: New York, 1978.
(23) Latimer, W. M. *Oxidation Potentials*, 2nd ed.; Prentice Hall: Englewood Cliffs, NJ, 1952.
(24) LaCourse, W. R.; Hsiao, Y.-L.; Johnson, D. C. *J. Electrochem. Soc.* **1989**, *136*, 3714.